

## Pore occupancy, relative permeability and flow intermittency measurements using X-ray micro-tomography in a complex carbonate

Ying Gao<sup>a,b,\*</sup>, Ali Qaseminejad Raeini<sup>a</sup>, Martin J. Blunt<sup>a,b</sup>, Branko Bijeljic<sup>a,b</sup>

<sup>a</sup> Department of Earth Science and Engineering, Imperial College London, London SW7 2AZ, United Kingdom

<sup>b</sup> Qatar Carbonates and Carbon Storage Research Centre, Department of Earth Science and Engineering, Imperial College London, London SW7 2AZ, United Kingdom



### ARTICLE INFO

#### Keywords:

Micro-CT imaging  
Two-phase flow  
Micro-porosity  
Relative permeability  
Intermittency  
Differential imaging

### ABSTRACT

We imaged the steady-state flow of brine and decane (oil) at different fractional flows during dual injection in a micro-porous limestone, Estaillades, using X-ray micro-tomography. We applied differential imaging to: (a) distinguish micro-porous regions from macro-pores, and (b) determine fluid pore occupancy in both regions, and relative permeability at a capillary number,  $Ca = 7.3 \times 10^{-6}$ . The sample porosity was approximately 28%, with 7% in macro-pores and 21% in pores that could not be directly resolved (micro-porosity). Fluid occupancy in micro-porosity was classified into three sub-phases: micro-pore space with oil, micro-pore space with brine, and micro-pores partially filled with oil and brine. Our method indicated an initially higher oil recovery from micro-porosity, consistent with waterflooding in a water-wet rock. The fractional flow and relative permeabilities of the two fluids were obtained from measurements of the pressure differential across the sample and the saturation calculated from the images. The brine saturation and relative permeabilities are impacted by the presence of water-wet micro-porosity which provides additional connectivity to the phases. Furthermore, we find that in addition to brine and decane, a fraction of the macroscopic pore space contains an intermittent phase, which is occupied either by brine or decane during the hour-long scan time. Pore and throat occupancy of oil, brine and intermittent phase were obtained from images at different fractional flows using the generalized pore network extracted from the image of macro-pores. The intermittent phase, where the occupancy fluctuated between oil-filled and brine-filled, was predominantly located in the small and intermediate size pores and throats. Overall, we establish a new experimental methodology to: (i) quantify initial and recovered oil in micro-pores, (ii) characterise intermittent flow, and (iii) measure steady-state relative permeability in carbonates, which is shown to be greatly influenced by micro-porosity.

### 1. Introduction

Carbonates are known to have a complex pore space whose heterogeneous structure and connectivity have a significant impact on flow, transport and reactive properties (Gouze et al., 2008; Bijeljic et al., 2013; Norouzi Apourvari and Arns, 2016). In particular, micro-porosity, while it may control the flow and transport behaviour, is challenging to describe using current imaging and modelling methods (Ghous et al., 2007; Tian and Wang, 2018).

X-ray computed micro-tomography (micro-CT) has been used to image multiphase flow configurations in geologically related studies. Complex pore-scale phenomena in carbonates have been captured at reservoir conditions and related petrophysical parameters measured directly in the pore space (Arns et al., 2005; Akbarabadi and Piri, 2013; Blunt et al., 2013; Wildenschild and Sheppard, 2013; Mahani

et al., 2015). When combined with an appropriate image processing method, the wealth of information on multi-fluid distributions in complex pore geometries can be obtained directly from a micro-CT experiment.

Recently, an improved understanding of the role of micro-porosity in single-phase flow in carbonates (Lin et al., 2016; Bijeljic et al., 2018) and two-phase flow in a dual porosity sandstone (Lin et al., 2017) has been provided using differential imaging micro-tomography. Importantly, the differential imaging method provides information on additional connectivity between macro-pores through micro-porosity. The quantification of micro-porosity can then be used in modelling studies (Bijeljic et al., 2018; Tian and Wang, 2018). Furthermore, differential imaging was used during steady-state two-phase flow in Bentheimer sandstone (Gao et al., 2017), in which an intermittent phase was distinguished in the macroscopic pore space which was periodically occupied by

\* Corresponding author at: Department of Earth Science and Engineering, Imperial College London, London SW7 2AZ, United Kingdom.

E-mail address: [y.gao15@imperial.ac.uk](mailto:y.gao15@imperial.ac.uk) (Y. Gao).

either oil or brine. This method is designed to capture rapid displacements during the comparatively slow micro-CT scan. In this work we will combine these two applications of differential imaging to study two-phase flow in a micro-porous carbonate, for which the pore space is more complex.

Multiphase flow is controlled by the balance between capillary and viscous forces which is impacted by several factors, including wettability and pore structure (Blunt, 2017). Different flow regimes are characterized by the ratio of viscous to capillary forces conventionally described by the capillary number,  $Ca = \mu v / \sigma$ , where  $\mu$  is the mean viscosity of the flowing phases,  $v$  is the total Darcy velocity, and  $\sigma$  is the interfacial tension. At sufficiently low  $Ca$  both oil and the aqueous phase (water or brine) flow through unchanging, distinct and connected pathways; in contrast, the non-wetting fluid is broken up into discrete ganglia at sufficiently high  $Ca$  (Chatenier and Calhoun Jr., 1952; Payatakes, 1982; Avraam and Payatakes, 1996; Tallakstad et al., 2009). This behaviour can be encapsulated in a phase or regime diagram (Datta et al., 2014a, 2014b; Armstrong et al., 2016). Using fast synchrotron imaging, at high  $Ca$ , ganglion dynamics was observed in a sandstone (Rücker et al., 2015a). Furthermore, Reynolds et al. (2017) observed dynamic changes in connectivity even at low  $Ca$  in a Bentheimer sandstone. Gao et al. (2017) also observed intermittent pore occupancy of brine and decane during simultaneous injection in the pore space of Bentheimer sandstone for  $Ca = 7.5 \times 10^{-6}$ . Pak et al. (2015) studied displacement in a complex carbonate and showed how large trapped ganglia of the non-wetting phase are broken up for  $Ca > 10^{-5}$ . However, the role of micro-porosity on the pore-scale displacement dynamics has not been explored.

Relative permeability describes the averaged flow behaviour of immiscible fluids and is used to predict field-scale oil recovery, carbon dioxide storage and contaminant transport. Compared with the expensive and time consuming conventional measurement of relative permeability at the cm-scale using steady state or unsteady state methods (Johnson et al., 1959; Kokkedee et al., 1996), pore-scale imaging not only provides insights into displacement processes, but the flow experiments can be faster since the volume investigated is typically smaller than a standard core sample. Turner et al. (2004) and Hussain et al. (2014) computed the relative permeability from the fluid distribution imaged during a displacement when flow was stopped during scanning. The same approach was employed using fluid distributions found from a synchrotron imaging imbibition experiment in a water-wet sandstone without stopping flow (Berg et al., 2015, 2016; Rücker et al., 2015b). However, the relative permeabilities were not directly measured from the pressure drop across the sample, but inferred from a flow computation on the image, which may introduce considerable uncertainties for the case of carbonates, where it is challenging to resolve all the pore space explicitly. Aghaei and Piri (2015) measured and computed the relative permeability from micro-CT images for both drainage and imbibition experiments in a water-wet sandstone. Zou et al. (2018) extended this work to study a mixed-wet sandstone and to explore the pore-scale displacement dynamics. However, these studies did not consider carbonate rocks, with complex pore geometries and significant micro-porosity (Gharbi and Blunt, 2012; Blunt et al., 2013; Ott et al., 2015; Prodanović et al., 2015).

In our previous work (Gao et al., 2017; Lin et al., 2018), we developed a method based on differential imaging to visualise flow regimes both at low and high  $Ca$  combined with a direct measurement of relative permeability for Bentheimer sandstone. As mentioned previously, intermittent pore occupancy was observed at high flow rates. In this paper, we examine pore occupancy in two-phase flow in the complex pore space of Estailades carbonate, with significant sub-resolution micro-porosity. Our goal is to examine the impact of micro-porosity on fluid distribution and relative permeability, measured directly from the pressure differential at different fractional flows (the ratio of brine flow rate to the total flow rate of oil and brine) during a steady-state experiment.

## 2. Experimental methodology

### 2.1. Rock samples and fluid properties

The sample used here is Estailades carbonate, which contains approximately 97.9% calcite and 2.1% quartz (analysis conducted at Weatherford Laboratories, East Grinstead, UK). The sample, called a core, was a cylinder  $6.01 \pm 0.01$  mm in diameter and  $51.34 \pm 0.01$  mm in length. The absolute permeability of the same sample was found from Darcy's law and the pressure differential measured at two flow rates, 0.2 mL/min and 0.5 mL/min, to be  $1.06 \pm 0.02 \times 10^{-13}$  m<sup>2</sup>. The total porosity, estimated from the micro-CT image in Section 3.2, was  $28.4 \pm 0.5\%$  of which micro-porosity accounted for 21.5%, while the macro porosity was 6.9%. The helium porosity of the same sample was  $30.3 \pm 0.2\%$ ; the image-based value is slightly lower, indicating that some micro-porosity was not captured.

The non-wetting phase was decane that has a density of 730 kg/m<sup>3</sup> (n-Decane, Acros Organics) and a viscosity of 0.838 mPa s (provided by PubChem, open chemistry database). To provide an optimal contrast between brine, oil and rock phases, 30 wt% potassium iodide (KI) brine was used as the wetting, aqueous, phase. The density of brine was measured to be  $1263 \pm 2$  kg/m<sup>3</sup> at ambient conditions by weighing a 1 mL drop of the liquid. The viscosity of brine is  $0.82 \pm 0.01$  mPas. Using the pendant drop method (Andreas et al., 1938; Stauffer, 1965), the interfacial tension between brine and decane was measured to be  $47 \pm 2$  mN/m at ambient conditions by a Ramé-Hart apparatus (590 F4 series).

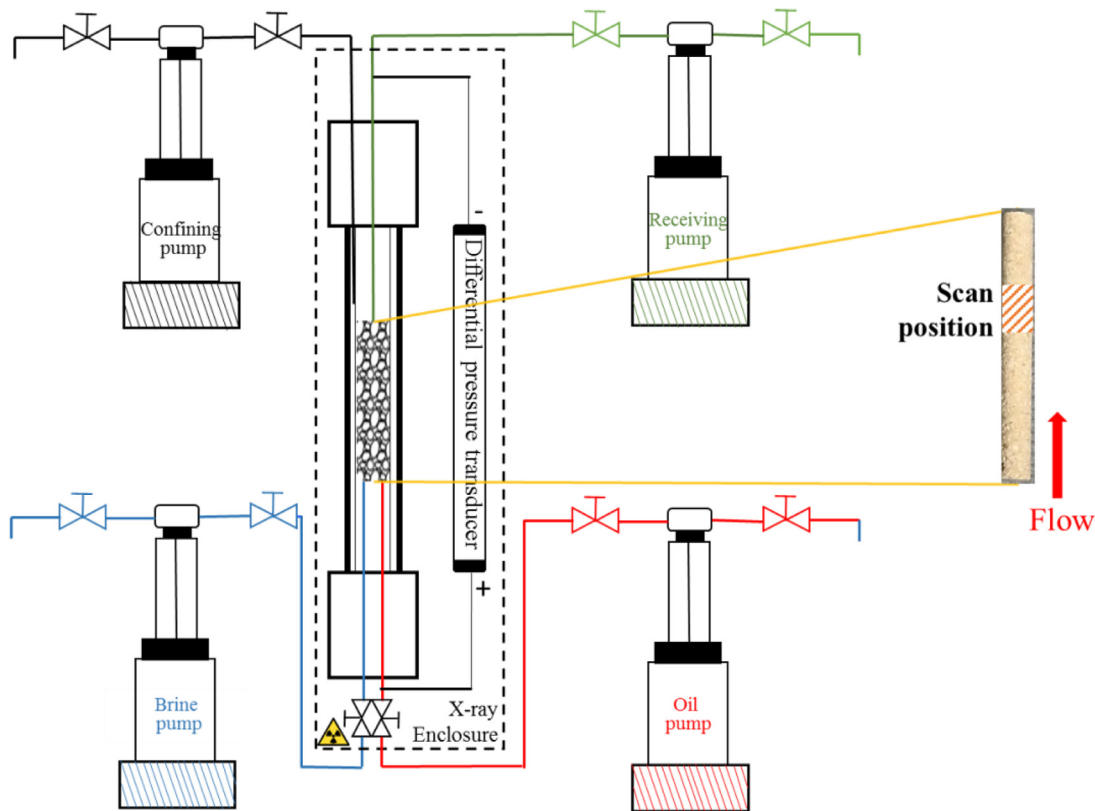
### 2.2. In situ X-ray tomography methodology

Fig. 1 shows our experimental design. We used a Hassler type flow cell made of carbon fibre around 1 mm thick that is transparent to X-rays. The Estailades sample was placed in a fluoro-polymer elastomer (Viton) sleeve approximately 1 mm thick and metal fittings at both ends were used to connect the core to the fluid flow-lines. Brine and decane were injected through two separate ports to ensure that two fluids flowed into the sample simultaneously.

The total flow rate of this experiment was 0.7 mL/min, which was kept fixed during the whole experiment at various fractional flows. The capillary number was calculated from the total flow rate. The viscosity used in the calculation of capillary number is the mean value of oil and brine viscosities. Thus the capillary number for this experiment was  $7.3 \times 10^{-6}$ . The fractional flow was defined as the volumetric injection rate of the aqueous phase divided by the total fluid rate of both the oil and aqueous phases:  $f_w = q_w / q_t$ , where  $q_w$  is the aqueous (brine) phase Darcy velocity and  $q_t$  is the total velocity. The capillary number is at the upper end of that encountered in reservoir settings and was chosen so that some intermittent flow would be observed, based on our previous work in a sandstone (Gao et al., 2017).

The experiments were performed using the following procedure:

1. A confining pressure of 2 MPa was established within the cell to compress the Viton sleeve outside the sample to prevent any fluid bypass. Two dry (air) scans were taken of the upper and lower parts of the core over a period of 80 min at ambient conditions. The overlap between the scans was approximately 25%. This overlap was used to stitch the two scans together.
2. CO<sub>2</sub> was injected into the rock sample for more than 30 min to replace the air.
3. Brine was injected and the sample was fully saturated with brine. A differential pressure transducer (PD-33X, Keller) was installed along the tubing. The "+" linked to the tubing at the inlet of the core holder and the "-" linked to the tubing of the outlet of core holder. The tubing between the main flow line and the transducer remained full of brine during the experiment and it was assumed that the transducer measured the pressure difference in the brine phase. The range of



**Fig. 1.** The experimental flow diagram. The pumps were used to control the flow and the core holder of the flow cell was placed in the micro-CT scanner. The Estaillades core sample is shown on the right. Scans were taken near the top of the core as shown. The “+” is linked to the tubing at the inlet of the core holder and the “-” linked to the tubing of the outlet of core holder.

the differential pressure transducer was 50,000 kPa, and the accuracy was 0.05% for the whole range.

4. More than 1000 pore volumes of brine were flushed into the sample at 1 mL/min to ensure the rock was fully filled with brine. 1000D high pressure syringe pumps were used to inject both oil and brine (Teledyne Isco Syringe Pumps). The flow range of the pump was from 0.1 mL/min to 408 mL/min, and the accuracy was  $\pm 0.5\%$ .
5. Two brine scans lasting 80 min were taken at the same position as the dry scans. A back pressure of 2000 kPa was set for the whole system.
6. Oil was injected (primary drainage) at a high flow rate of 2 mL/min for 30 min to obtain a uniform initial brine saturation.
7. Oil injection was continued at a flow rate of 0.7 mL/min, while the brine fractional flow was 0. Injection continued until the flow reached steady state, which could be recognized by observing a stable and constant pressure drop for more than 2 h. In our experiment it took approximately 20 h to reach steady state. Then scans were taken at the same position of the core over a period of 80 min without stopping the flow.
8. Step 7 was repeated for fractional flows,  $f_w$ , of 0.15, 0.3, 0.5, 0.7 and 0.85. While keeping the total volumetric flow rate fixed, the oil flow rate decreased from 0.595 mL/min to 0.105 mL/min and the brine flow rate increased from 0.105 mL/min to 0.595 mL/min. This whole process was an imbibition displacement in this water-wet sample (brine was the wetting phase). At the same time, the pressure drop across the whole sample was recorded during the experiment. It took approximately 16–25 h for each fractional flow experiment to reach steady state. Two scans were taken at the same

position of the core over a period of 80 min without stopping the flow.

9. High flow rate (2 mL/min) brine injection was performed for 30 min to reach the residual oil saturation. Then brine injection continued at 0.7 mL/min to measure the steady-state pressure difference when the fractional flow was 1.
10. After cleaning all the tubing and end fittings used in the experiment, steps 7 to 9 were applied to the whole system without the rock sample. The pressure drops of the tubing itself were recorded at all fractional flows, which ranged from 2 kPa to 20 kPa. The lowest pressure drop was obtained when  $f_w$  was 0, while the largest was obtained when  $f_w$  was 0.85.
11. The pressure differences along the cores were calculated by subtracting the pressure drops along the tubing measured at step 10 from the total pressure drops measured from steps 7 to 9.

The fluid configurations were imaged using a Zeiss XRM-510 X-Ray microscope at a voxel size of  $3.58 \mu\text{m}$  using a flat panel detector. The X-ray energy was 75 keV, the exposure time was 0.5 s and the number of projections was 1601. All these projections were reconstructed into a three-dimensional image using proprietary software on the Versa system. Two images were taken and then stitched together to obtain a larger field of view to analyse. Then the stitched images were cropped into cylindrical sections to avoid the sleeve shown at the boundaries of the core. The stitched image size was  $1582 \times 1582 \times 2789$  voxels, 5.66 mm in diameter and 9.98 mm in length, which represents a bulk volume of  $251.1 \text{ mm}^3$ . All reconstructed images were registered to the dry scan image to have the same orientation, and the Lanczos algorithm was used to resample them (Burger and Burge, 2016).

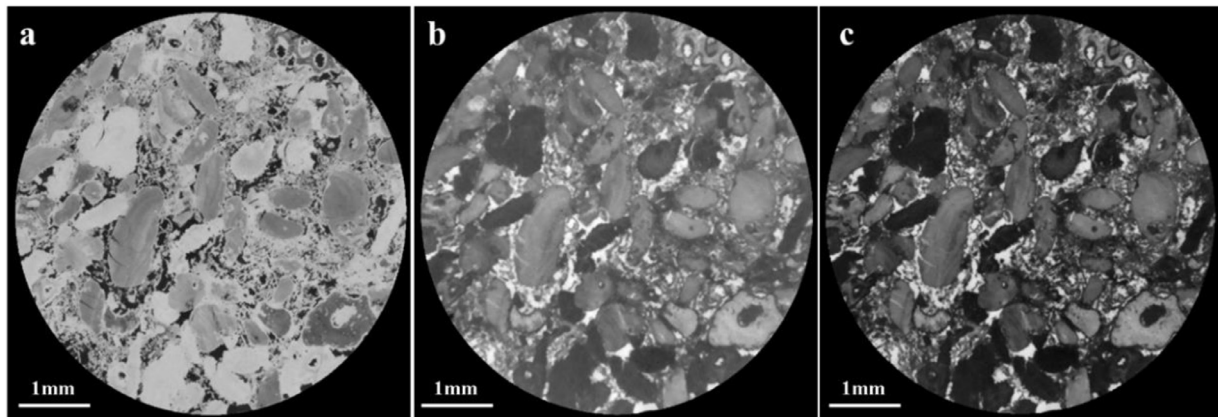


**Fig. 2.** Two-dimensional cross-sections of three-dimensional micro-CT images at the same location in the Estaillades sample. (a) The dry scan. Air in the pore space does not adsorb X-rays and is black in the image. (b) The brine-saturated image. Brine has a higher X-ray attenuation than solid and appears bright (white) in the image. (c) The difference image between (b) and (a). The black in (c) represents impermeable solid grains, white is macro-pore space, while intermediate grey values indicate micro-porosity where the pore structure cannot be explicitly resolved in the image.

### 3. Results and discussion

We first present the differential imaging method used to distinguish micro- and macro-pore space in [Section 3.1](#). Then in [Sections 3.2](#) and [3.3](#) we demonstrate how to quantify the fluid occupancy in the micro- and macro-pore space using the differential imaging method. Furthermore, in [Section 3.4](#) we study change in fluid occupancy with fractional flow, while the associated steady-state relative permeability measurements are presented in [Section 3.5](#). In [Section 3.6](#) we quantify and examine the intermittent phase dependence on pore and throat size.

#### 3.1. Characterization of micro- and macro-pore space

In contrast to the earlier studies on sandstones, Estaillades carbonate has a bimodal pore structure with inter-granular macro-porosity and micro-porosity, whose pore throat radius distribution clearly shows two peaks around 0.2 and 10  $\mu\text{m}$  from mercury injection capillary pressure analysis ([Bijelic et al., 2013; Alyafei and Blunt, 2016](#)), as shown in the cross-sectional images in [Fig. 2](#). [Fig. 2a](#) and [b](#) show the images of the dry scan and the scan of the sample saturated with 30wt% KI brine, respectively. We have designed the experiment so that brine has the strongest X-ray adsorption – even greater than solid – and appears bright (white) in the raw images. Using the differential imaging method, we subtract the dry scan from the brine scan to distinguish micro-porosity from macroscopic pore space. [Fig. 2c](#) is the difference image between [Fig. 2b](#) and [a](#), from which solid grain, macro-pore space and micro-porosity can be discriminated. A non-local means filter was applied on the differential images to reduce the noise while preserving edges ([Buades et al., 2005, 2008](#)). Then intensity-based thresholding was used to segment the image into different phases ([Lin et al., 2016](#)).

The histogram of the grey-scale CT numbers (which represents the X-ray attenuation) for the dry scan is presented in [Fig. 3](#). Here solid grain, micro-porous and macro-pore space can be distinguished, for which fluid occupancy is studied in [Sections 3.2](#) and [3.3](#).

#### 3.2. Fluid occupancy and porosity in the micro-pore space

Grey-scale images are illustrated in [Fig. 4](#), where two-dimensional cross-sections of three-dimensional raw micro-CT images over a range of fractional flows are presented. The grey represents grains and intermittent phase in macro-pores, as well as micro-porosity, the black is stable oil in macro-pores, while the white is brine in macro-pores.

The first observation is that there are some voxels in the micro-porous space which did not change grey-scale value for all fractional flows, indicating that they were always filled with brine. The second

observation is that, with increasing fractional flow, some voxels in the micro-porous space significantly increased their grey-scale value which became similar to the value of brine-only voxels; these are the regions which are indicated by the red circles. This shows that oil in the micro-porosity was displaced by brine.

Differential imaging can be used to discriminate the fluid occupancy in micro-porosity – separating the voxels filled only with brine, and the voxels that were partially filled by brine and oil. This fluid occupancy was then determined by calculating the difference image between the fully brine-saturated scan and the scan at each fractional flow.

Image normalization was then used to ensure that the grey-scale value of each voxel was the same for the images taken at different fractional flows if the fluid occupancy was unchanged. Thus the peak values of the grey-scale histogram distribution for multiphase images were rescaled to be the same as those of the brine saturated image. Then the difference image between the brine scan and the multiphase flow scan is defined as:

$$CT(\text{difference}) = CT(\text{brine scan}) - CT(\text{multiphase scan}) + CT0 \quad (1)$$

where  $CT$  is the CT number of each voxel, and  $CT0$  is a constant value to avoid negative grey-scale values. The difference images between the brine saturated scan and the multiphase flow scan clearly identify changes in fluid occupancy. [Fig. 5](#) shows the difference images at different fractional flows for this experiment: black represents solid grain phase and unchanged brine, while white indicates oil in macro-pores. There are also grey regions which can represent either an intermittent phase, indicating that some of the time these regions were oil-filled and at other times brine-filled during the scan time of 40 min, or oil in the micro-porous phase, as shown in the red circles.

##### 3.2.1. Determination of fluid occupancy-based porosity

Based on the analysis of oil and brine pore occupancy at all fractional flows, we found that 85.5% of the micro-pore space was saturated only with brine, see [Table 1](#). Oil did not occupy these pores because of the high capillary entry pressure. Hence, we distinguished four phases: solid grain, micro-pore phase I (always occupied by brine), micro-pore phase II (which contains both oil and brine), and macro-pore space, as shown in [Fig. 6](#).

The histograms of CT number for all grey-scale voxels in the dry image are plotted for each phase, as shown in [Fig. 7](#). The red curve represents solid grain phase, the green represents micro-pore phase I, the orange represents micro-pore phase II and the blue represents macro-pore phase. In the dry image, the contribution to the total porosity, from

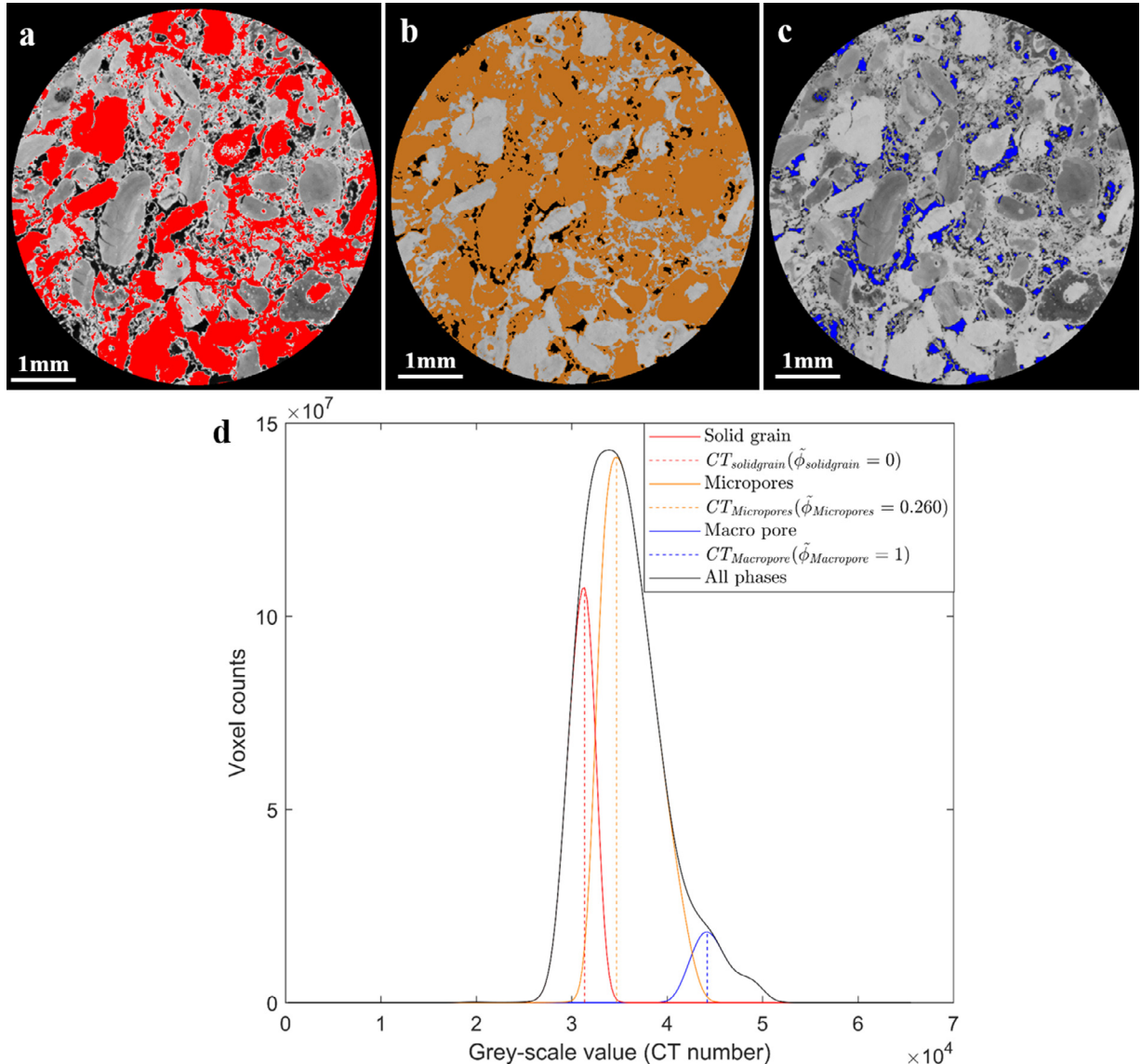


**Fig. 3.** (a)–(c) Segmentation classification shown as two-dimensional cross-sections of the three-dimensional images of the same slice: (a) Solid grains (red). (b) Micro-pore phase (orange). (c) Macro-pore space (blue). (d) The histograms for the different phases found in the brine scan after image segmentation. The red line represents the solid phase, the orange line represents the micro-porous phase and the blue line represents the brine phase. The dashed lines indicate the grey-scale values at the peak of each phase histogram. (For interpretation of the references to colour in this figure legend, the reader is referred to the web version of this article.)

**Table 1**

Volume fraction of solid grain, micro-pore space I, micro-pore space II and macro-pore space, and the corresponding porosity ( $i$  represents the phase  $i$ ).

Type	Volume fraction $p_i$	Porosity $\tilde{\phi}_i$	Contribution to total porosity $\phi_i$
Solid grain	0.267	0	0
Micro-pore space I	0.568	0.260	0.148
Micro-pore space II	0.096	0.700	0.067
Macro-pore space	0.069	1	0.069
Total porosity			0.284

micro-pore phase II was estimated as:

$$\phi_{microporeII} = p_{microporeII} \tilde{\phi}_{microporeII} = p_{microporeII} \frac{CT_{microporeII} - CT_{solidgrain}}{CT_{macropore} - CT_{solidgrain}} \quad (2)$$

where  $\phi_{microporeII}$  is the porosity contribution of micro-pore phase II,  $p_{microporeII}$  is the fraction of the micro-pore phase II to the total volume

(including grains),  $\tilde{\phi}_{microporeII}$  is the porosity of the micro-pore phase II, which was calculated to be 0.70 in this sample. The grey-scale values where the peak values are located for each pore space in the histogram are denoted as  $CT_{solidgrain}$  for the solid grain phase,  $CT_{microporeI}$  for the micro-pore phase I (occupied by brine only),  $CT_{microporeII}$  for the micro-pore phase II (occupied by brine and/or oil), and  $CT_{macropore}$  for the macro-pore phase.

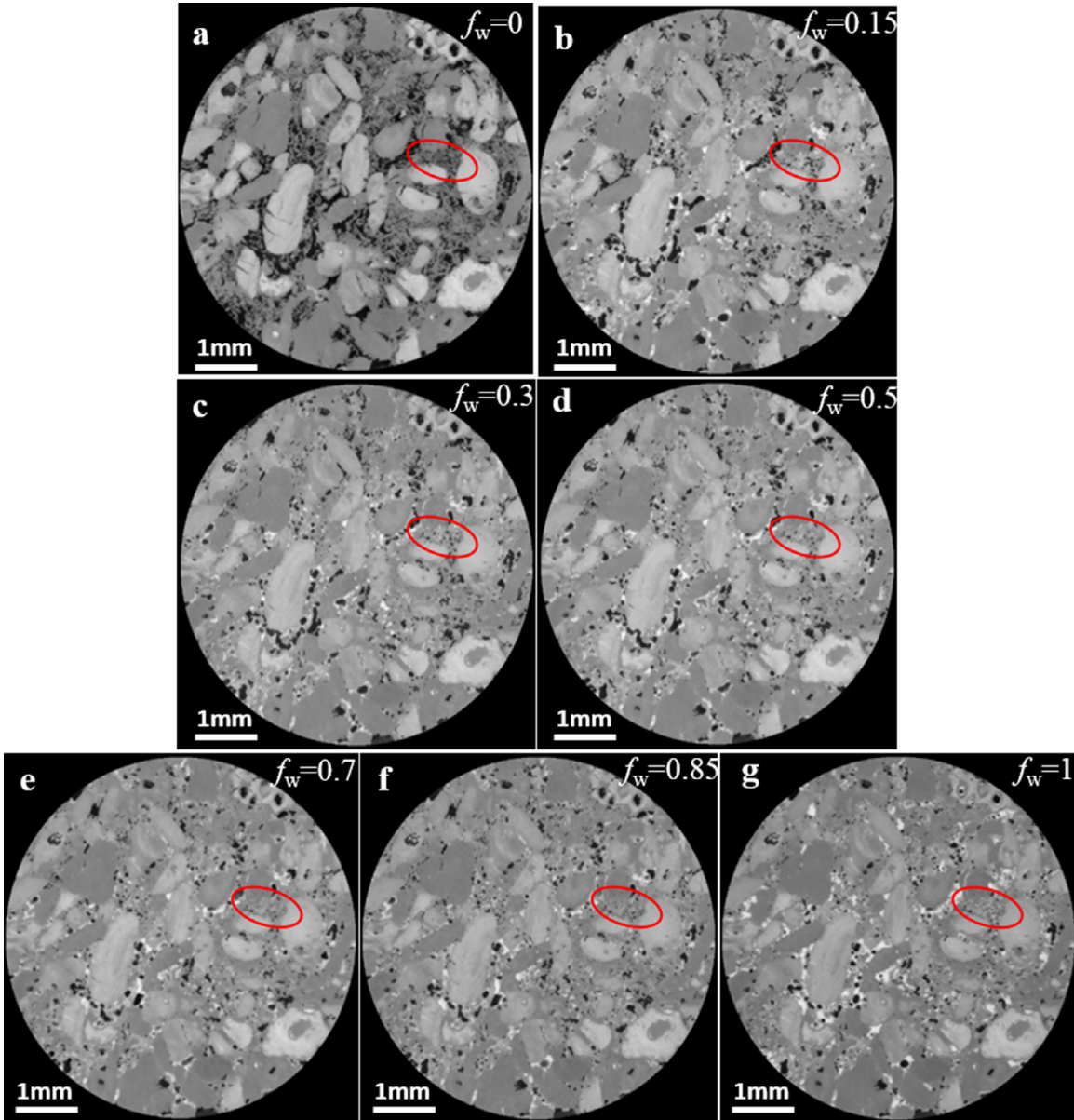


**Fig. 4.** Two-dimensional cross-sections of three-dimensional micro-CT images of the same slice at different fractional flows. From left to right and from top to bottom, the fractional flow is 0, 0.15, 0.3, 0.5, 0.7, 0.85, and 1. The grey includes grain, micro-porosity and intermittent phase in macro-pores, the black represents stable oil in macro-pores which adsorbs X-rays the least, and the white is brine in macro-pores which has the strongest X-ray adsorption. The red circles show areas where oil was displaced by brine in the micro-porosity. (For interpretation of the references to colour in this figure legend, the reader is referred to the web version of this article.)

The porosity of each phase measured using the differential imaging method is shown in Table 1.

### 3.2.2. Fluid occupancy in micro-pore space

Flow heterogeneity in carbonates is affected by the presence of micro-porosity. Using the differential imaging method, we now distinguish pore occupancy in the microscopic pore space. The raw images were segmented based on the four-phase masks shown in Fig. 6 and the difference images shown in Fig. 5. Furthermore, oil, brine and partially filled micro-pores were segmented based on the grey-scale distribution histogram of micro-pore space II, shown in Fig. 8. In the multiphase images the contribution to the brine saturation in the partially filled micro-pores was estimated as:

$$S_{w\_PF\_microporeII} = \phi_{PFM} \tilde{S}_w = \phi_{PFM} \frac{CT_{PF\text{micropores}} - CT_{oil}}{CT_{brine} - CT_{oil}} \quad (3)$$

where  $S_{w\_PF\_microporeII}$  is the contribution to the brine saturation in partially filled micro-pores in micro-pore space II,  $\phi_{PFM}$  is the fraction of the partially filled micro-pore space to the total pore volume of micro-pore space II. The grey-scale values where the peak values are located for each phase in the histogram are denoted as  $CT_{Oil}$  for the oil in micro-pore space II,  $CT_{PF\text{micropores}}$  for the partially filled micro-pores, and  $CT_{Brine}$  for the brine in micro-pore space II.

For a fractional flow of 0.5, the fraction of brine in partially filled micro-pore space is 0.333 (shown in Fig. 8) and the fraction of the partially filled micro-pores in total pore space is 0.192 (shown in Table 2), so the contribution to the total brine saturation from partially filled micro-pores in micro-pore space II is the product of these two numbers giving the value of 0.064. Fluid occupancy in micro-pore space for all fractional flows is provided in Table 2.

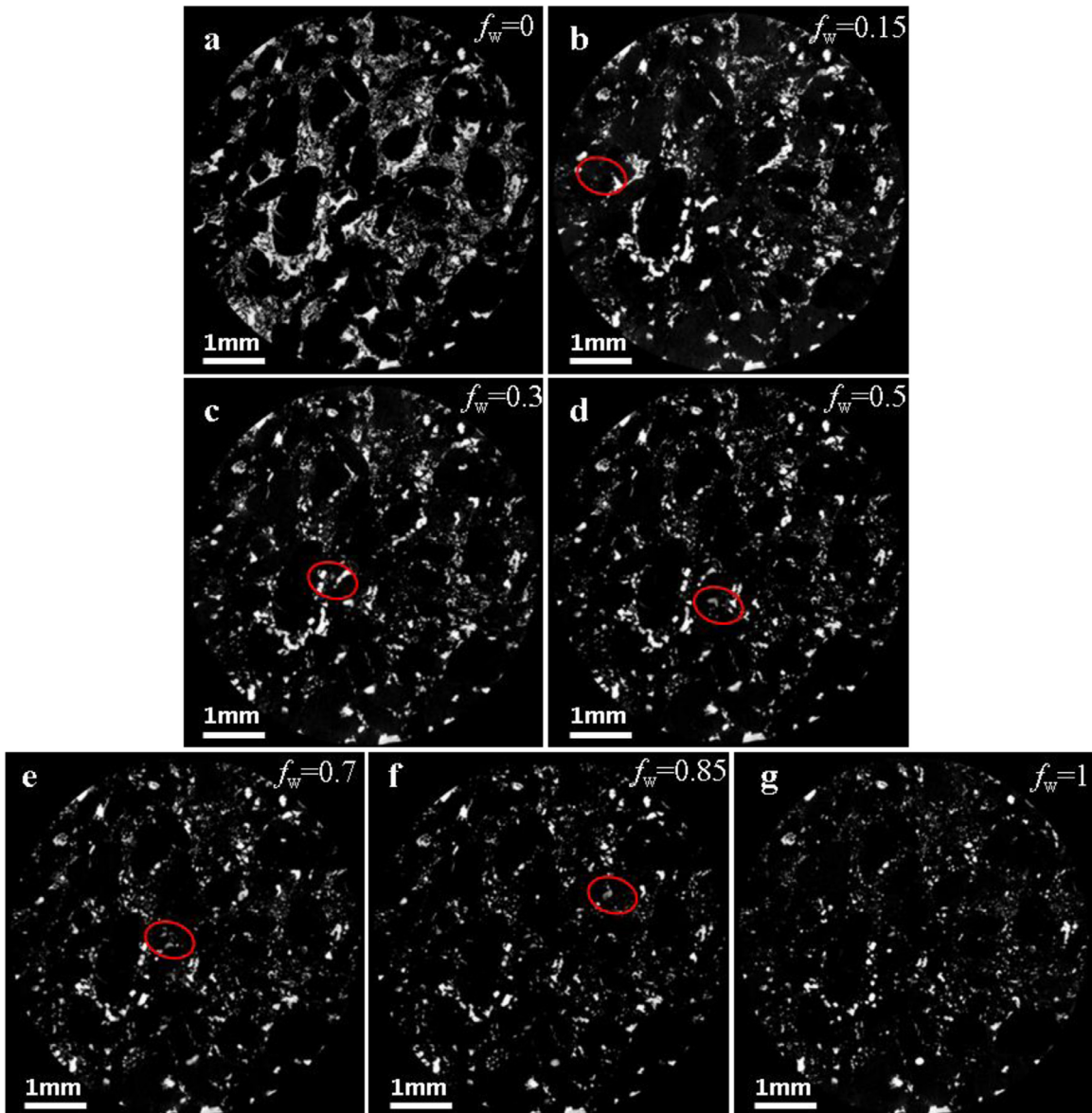


**Fig. 5.** Two-dimensional cross-sections of three-dimensional difference images of the same slice. From left to right and from top to bottom, the fractional flow is 0, 0.15, 0.3, 0.5, 0.7, 0.85, and 1. Black indicates solid grains and brine in the multiphase scans. White represents oil in the macro-pores. Grey represents either oil in micro-porosity (indicated by the red circles), or an intermittent phase (fluctuating pore occupancy of brine and oil) in the macro-pores.

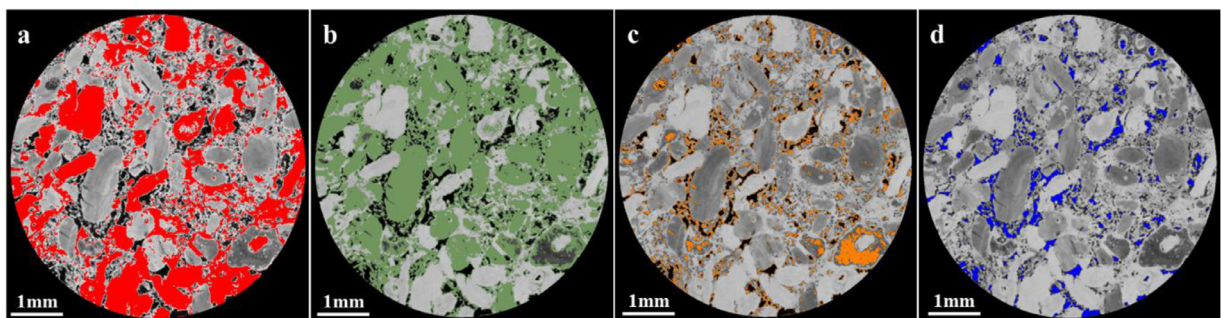


**Fig. 6.** Segmentation classification shown on two-dimensional cross-sections of the three-dimensional images of the same slice. (a) Solid grain (red). (b) Micro-pore phase I (green), which is always saturated with brine. (c) Micro-pore phase II, which contains both oil and brine (orange). (d) Macro-pore space (blue), which can be saturated with either oil or brine. (For interpretation of the references to colour in this figure legend, the reader is referred to the web version of this article.)

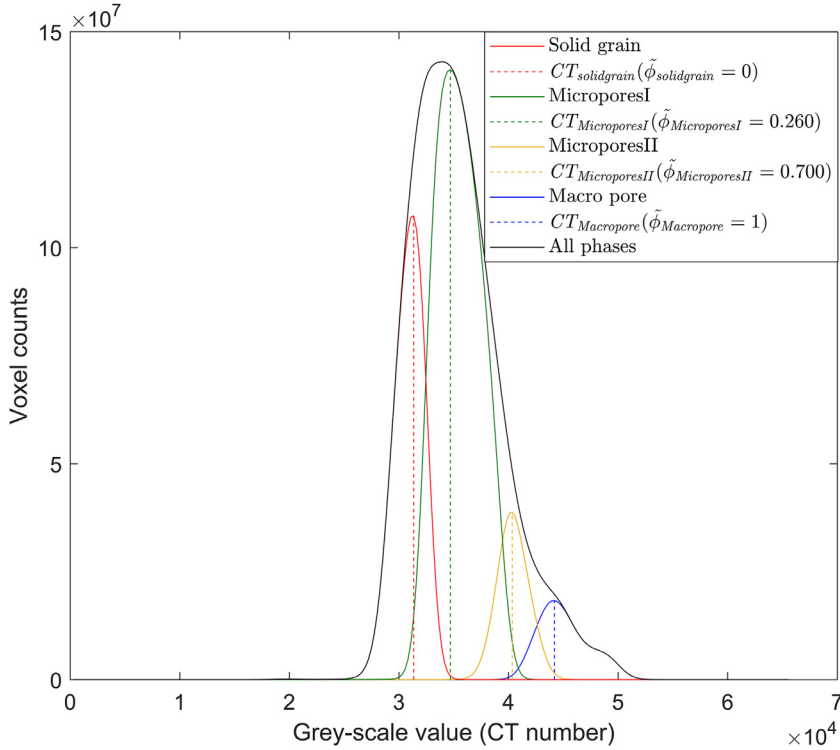


**Fig. 7.** The histograms for the different phases of the brine scan. The red curve represents solid grain phase, the green represents micro-pore phase I, the orange represents micro-pore phase II and the blue represents macro-pore phase. The red dashed line indicates the grey-scale value of the peak of the histogram for solid grain phase, the green dashed line indicates the grey-scale value of the peak of the histogram for the micro-pore phase I, the orange dashed line indicates the grey-scale value of the peak of the histogram for the micro-pore phase II, and the blue dashed line shows the grey-scale value of the peak of the histogram for the macro-pore phase. (For interpretation of the references to colour in this figure legend, the reader is referred to the web version of this article.)

**Table 2**

Fractions of oil and brine in macro- and micro-pores for the different fractional flows studied.

$f_w$	$Ca = 7.3 \times 10^{-6}$							
	$S_w$	Fraction of the macro-pore space containing stable oil	Fraction of the macro-pore space containing stable brine	Fraction of the macro-pore space containing intermittent phase	Fraction of micro-pore phase II that is partially filled	Fraction of micro-pore phase II filled with oil	Fraction of micro-pore phase II filled with brine	The brine saturation $S_w$ from micro-pore phase I
0	0.588	0.988	0.012	0.000	0.000	0.723	0.277	0.521
0.15	0.702	0.753	0.115	0.132	0.170	0.307	0.523	0.521
0.3	0.720	0.666	0.128	0.206	0.142	0.299	0.559	0.521
0.5	0.765	0.578	0.185	0.237	0.192	0.191	0.617	0.521
0.7	0.779	0.564	0.181	0.255	0.194	0.186	0.620	0.521
0.85	0.781	0.513	0.276	0.211	0.164	0.177	0.659	0.521
1	0.855	0.362	0.638	0.000	0.000	0.240	0.760	0.521

### 3.3. Fluid occupancy in the macro-pore space

The differential image, shown in Fig. 5, was segmented to obtain the oil phase (white), and the intermittent phase (grey) in the macro-pores. Then the brine phase was obtained by subtracting the oil and intermittent phase from the macro-pore phase. The fluids in the macro-pores, shown in Fig. 9, was segmented into brine (blue), oil (red) and intermittent (yellow) phases.

Using these segmented label images as a reference, separate raw images for each phase were extracted. Fig. 10 shows the histograms of the grey-scale values of the image at a fractional flow of 0.5, for the oil, brine and intermittent phase of the macro-pore space. In the macro-pore space, the contribution of the intermittent phase in the macro pores to the brine saturation was estimated as:

$$S_{w\_inter\_macropore} = \phi_{inter} \tilde{S}_w = \phi_{inter} \frac{CT_{intermittency} - CT_{oil}}{CT_{brine} - CT_{oil}} \quad (4)$$

where  $S_{w\_inter\_macropore}$  is the contribution of the intermittent phase to the brine saturation, and  $\phi_{inter}$  is the fraction of the intermittent phase to the total pore volume. The grey-scale values where the peak values are located for each phase in the histogram were denoted as  $CT_{Oil}$  for

the stable oil phase,  $CT_{Intermittency}$  for the intermittent phase,  $CT_{Brine}$  for the stable brine phase, and  $\tilde{S}_w$  denotes the proportion of brine in the intermittent phase.

For illustration, for a fractional flow of 0.5, the fraction of brine in the intermittent phase is 0.470 (shown in Fig. 10) and the fraction of the intermittent phase in total pore space is 0.237 (shown in Table 2), hence the contribution to the total brine saturation in the intermittent phase is 0.111. In the next section we provide fluid occupancy in the macro-pore space for all fractional flows.

### 3.4. Fluid occupancy in the macro- and micro-pore space and dependence on fractional flow

The brine saturation in the micro-pore space, macro-pore space, and the total saturation along the image are shown in Fig. 11. The uncertainty in saturation averaged over each slice of the total pore space is approximately 3%, including 2% for micropores and 1% for macropores. The amount of brine in the macro-pore space was approximately constant. However, the fraction of brine in the micro-pore space varied along the image because Estaillades has a heterogeneous pore structure.

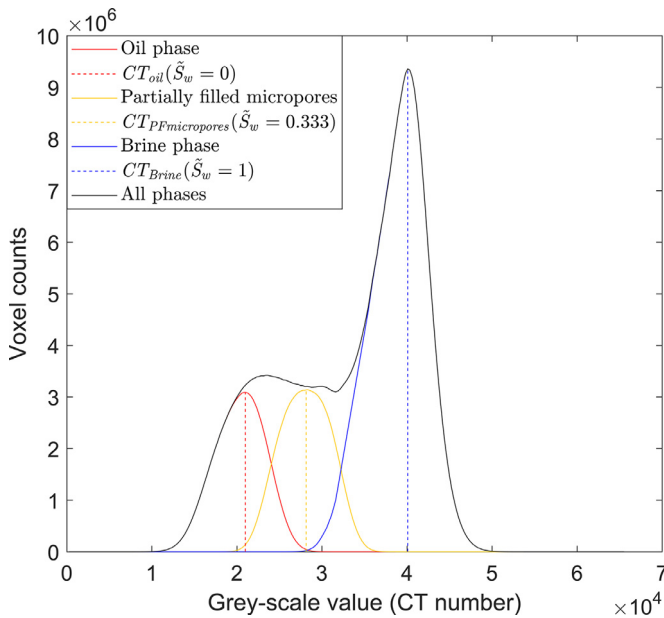


**Fig. 8.** Histograms of the grey-scale values for the oil, partially filled micro-pore, and brine phase in micro-pore space II when  $f_w = 0.5$ . The dashed lines in the histograms indicate the grey-scale values where the peaks for each phase exist. For the partially filled micro-pores the proportion of brine is 0.333 (calculated using Eq. (3)), while the contribution to the total brine saturation in partially filled micro-pores in micro-pore space II is 0.064.

Overall, the brine saturation was not uniform along the image because micro-porosity made a significant contribution to the total brine saturation.

From the profiles we observe that a considerable fraction of micro-porosity became occupied by brine that displaced oil when the fractional flow was initially increased from 0 to 0.15. Further increases resulted in a smaller oil displacement that is non-uniform along the core, reflecting the complex micro-porous space. These findings illustrate that in a water-wet rock, pore filling during waterflood occurs in order of increasing size, and hence the micro-porosity is preferentially filled first. This is further confirmed from the plots of remaining oil saturation in micro- and macro-pore space shown in Fig. 12. The normalised oil saturation decreased faster in the micro-porous regions with smaller pores until a fractional flow of 0.85.

Table 2 lists the fractions of oil and brine in the macro- and micro-porous regions.

### 3.5. Relative permeability

As mentioned in Section 2.2, the pressure difference across the rock sample at steady-state conditions was measured using the differential pressure transducer shown in Fig. 1. Fig. 13 shows the mean pressure differentials at different fractional flows during the last two hours, as well as the corresponding standard deviation. We have subtracted the pressure drop in the flow lines themselves (see step 10 of the experimental procedure in Section 2.2).

When the fractional flow was 0 and 1, the pressure profile was smooth, which indicates an unchanging fluid configuration. However, there were rapid pressure fluctuations during intermediate fractional flows, as observed previously (Sinha and Hansen, 2012; Sinha et al., 2017). For this experiment, the range of the fluctuations was from 0.55 kPa to 8.63 kPa. In the Bentheimer experiment at the same  $Ca$  (Gao et al., 2017), the range was from 0.12 kPa to 10.72 kPa. The pressure fluctuations are indicative of pore-scale rearrangements and have a magnitude equal to a typical capillary pressure, which is approximately

**Table 3**

Saturation and relative permeability calculated over a range of  $f_w$ .

$f_w$	$Ca = 7.3 \times 10^{-6}$			
	$S_w$	$k_{ro}$	$k_{rw}$	$\Delta p/kPa$
0	0.588	0.577	0.000	$289.99 \pm 0.55$
0.15	0.702	0.133	0.023	$1068.42 \pm 3.03$
0.3	0.720	0.097	0.041	$1204.41 \pm 8.63$
0.5	0.765	0.053	0.053	$1538.00 \pm 4.09$
0.7	0.779	0.032	0.075	$1540.52 \pm 2.54$
0.85	0.781	0.019	0.083	$1680.01 \pm 3.35$
1	0.855	0.000	0.274	$600.01 \pm 2.75$

12.5 kPa calculated from  $2\sigma/r$  where  $\sigma$  is the interfacial tension and  $r$  is the average throat radius of 7.5  $\mu m$  for Estaillades (Blunt, 2017).

The relative permeability was calculated by:

$$k_{rw} = \frac{q_w \mu_w L}{\Delta p k}; k_{ro} = \frac{q_o \mu_o L}{\Delta p k} \quad (5)$$

where  $k_{rw}$  is the brine relative permeability,  $k_{ro}$  is the oil relative permeability,  $\mu_w$  is the brine viscosity (Pa s),  $\mu_o$  is the oil viscosity (Pa s),  $q_w$  is the brine Darcy velocity (flow rate per unit area) (m/s),  $q_o$  is the oil Darcy velocity (m/s),  $L$  is the length of the whole sample (m),  $k$  is the absolute permeability ( $m^2$ ), and  $\Delta p$  is the pressure difference across the sample (Pa). We do not need to correct for capillary pressure gradients (the capillary end effect), as there is no discernable saturation gradient across the core, see Fig. 11 (Lin et al., 2018).

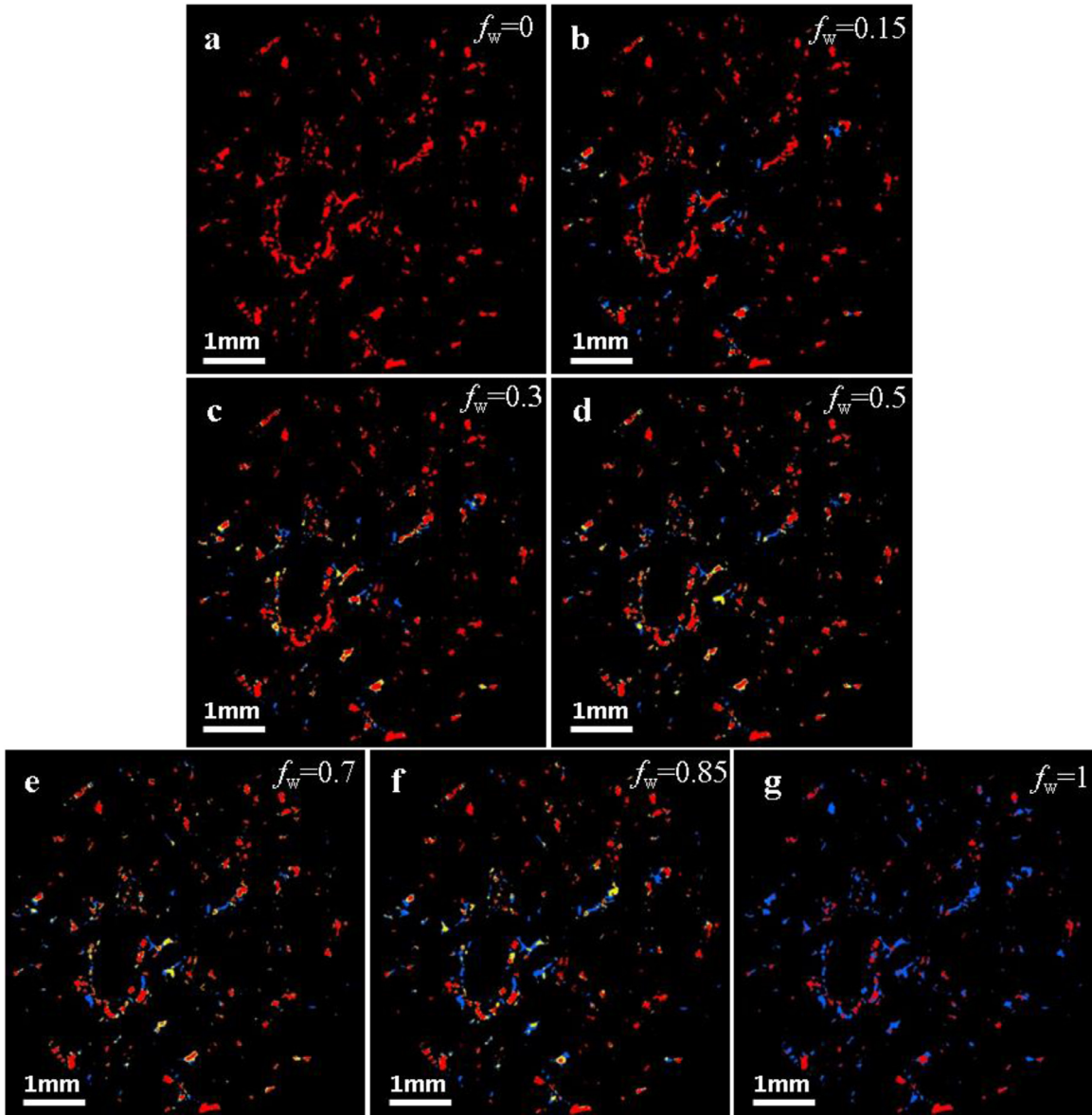
Table 3 shows the wetting phase saturation and the measured oil and brine relative permeabilities at each fractional flow. The saturation values shown in the table are calculated from the scanned region of the core.

Fig. 14 shows the estimated fractional flow curves at steady state for Estaillades carbonate studied here and Bentheimer sandstone measured in previous work (Gao et al., 2017) together with the relative permeabilities for these two rocks. The uncertainties in saturation are estimated from the root-mean square uncertainties in phase volume, total volume and porosity during image segmentation in both figures. The uncertainties in relative permeability consider uncertainties in the measurement of the length and diameter of the sample, the absolute permeability, pressure measurements, accuracy of the pressure transducers and the pump rates. At the end of primary drainage, the initial brine saturation for Estaillades was  $0.588 \pm 0.020$ , while at the end of imbibition, the residual oil saturation was  $0.145 \pm 0.016$ . The initial brine saturation for Bentheimer was  $0.145 \pm 0.031$ , while the residual oil saturation was  $0.337 \pm 0.030$ .

Both the sandstone and carbonate samples are strongly water-wet. The micro-porosity has a significant impact on the relative permeability of Estaillades carbonate. Since brine occupies micro-pores there is a considerable shift to higher brine saturations compared to Bentheimer sandstone. Moreover, the Estaillades water (brine) relative permeability rises more steeply and to higher values, which is an indication of the enhanced permeability and connectivity from micro-porous regions. The residual oil saturation is lower than in the sandstone; this is partly due to the higher initial brine saturation and also due to additional connectivity through oil-filled micro-porosity preventing complete disconnection of the oil. In contrast, the oil, that only occupies a small fraction of the micro-porosity, has a relative permeability that is similar in shape to the sandstone, albeit shifted to higher brine saturation.

### 3.6. Pore and throat occupancy of the intermittent phase

We now test the hypothesis that the existence of intermittent phase in the macroscopic pore space depends on pore and/or throat size. A generalized pore network extraction algorithm (Raeini et al., 2017) was used to subdivide macroscopic pore space into pores bounded by throat



**Fig. 9.** Three-phase segmented label image showing brine (blue), intermittent phase (yellow) and oil phase (red) in the macro-pore space. From left to right and from top to bottom, the fractional flow is 0, 0.15, 0.3, 0.5, 0.7, 0.85, and 1. (For interpretation of the references to colour in this figure legend, the reader is referred to the web version of this article.)

surfaces. Each voxel is assigned to a unique pore as well as to a unique throat (the closest throat surface). The volume of the pore and throat voxels, and their inscribed radii were used to analyse the statistics of the pore and throat fluid occupancy.

The pores and throats in the network were sorted based on their radii and divided into bins of equal volume. These bins are then used to compute the volume fraction of pores and throats, in each bin, whose centres were filled with oil, brine or the intermittent phase. Fig. 15 shows the results for different fractional flow images.

As expected for a water-wet (brine-wetting) medium, the oil occupies the larger pores while brine preferentially resides in small pores and throats. There is more brine in the throats than pores, as throats represent restrictions in the void space. However, brine is seen in some larger elements, and in general the tendency for brine to reside strictly in the smaller pores and throats is less marked than that observed in water-wet sandstones (Bultreys et al., 2018). In particular, when the oil is trapped (for  $f_w = 1$ ) we see oil and brine in elements of all sizes with only a weak preference for oil to remain in larger pores. The reason for

this is likely to be the presence of micro-porosity. As shown in Table 2, some oil also resides in the micro-porosity. Hence a much wider range of pore sizes are occupied by both phases than encountered typically in sandstones: the exact occupancy will be controlled by pore size, local pore geometry and connectivity, and we even see some oil trapped in the micro-porosity at the end of the experiment, Fig. 11.

As evident in Fig. 15, we mostly see the intermittent phase for intermediate fractional flows: for  $f_w = 0$  and  $f_w = 1$ , the flow paths are fixed, as only one phase is flowing. However, when both phases simultaneously flow through the rock, there are regions of the pore space where – during the period of the scan – sometimes oil is present and sometimes brine. This shows that the flow pathways are not fixed, but that a dynamic or intermittent connectivity is observed. This fluctuating occupancy has been seen directly using fast synchrotron imaging in Bentheimer sandstone (Reynolds et al., 2017). Intermittency has also been seen in Bentheimer at the same  $Ca$  and fluids as considered here (Gao et al., 2017). Compared to the sandstone, however, the fraction of the pores occupied by the intermittent phase in the carbonate was smaller. For example,

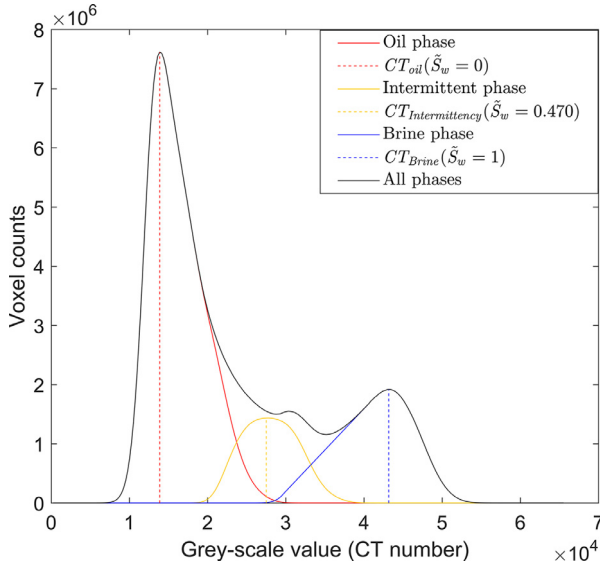


**Fig. 10.** The histograms for the different phases in macro-pore space when  $f_w$  is 0.5. The dashed lines in the histograms indicate the grey-scale values where the peaks for each phase exist. The proportion of brine in the intermittent phase is 0.470 (calculated using Eq. (4)), while the contribution to the total brine saturation in the intermittent phase in macro-pore space is 0.111.

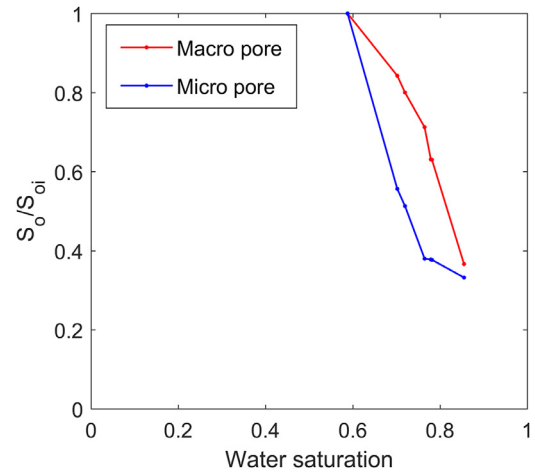


**Fig. 12.** Oil saturation normalised by initial oil saturation in the micro- and macro-pore space as a function of total water (brine) saturation.

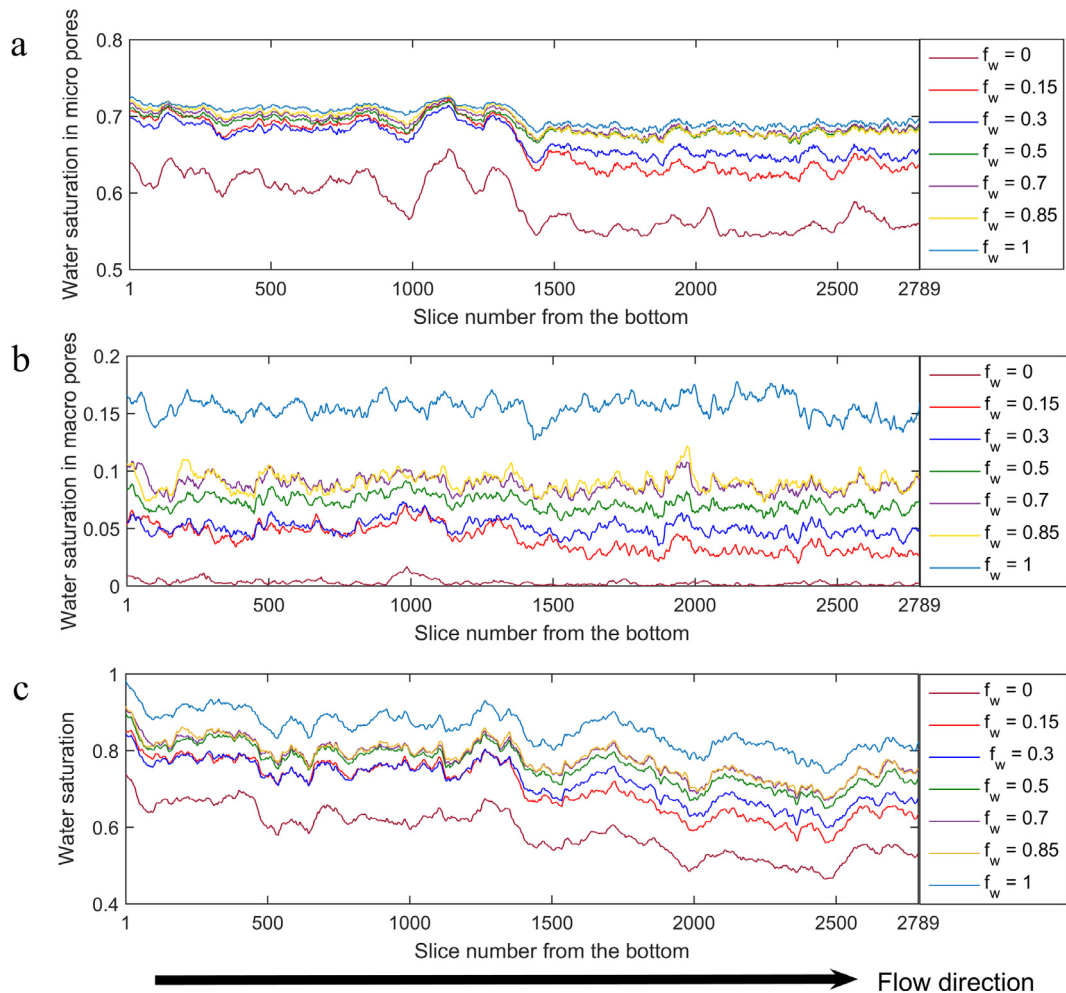


**Fig. 11.** Brine saturation profiles in micro-pores (a), macro-pores (b) and total saturation (c). From bottom to top on each graph, the fractional flow is 0, 0.15, 0.3, 0.5, 0.7, 0.85, and 1.

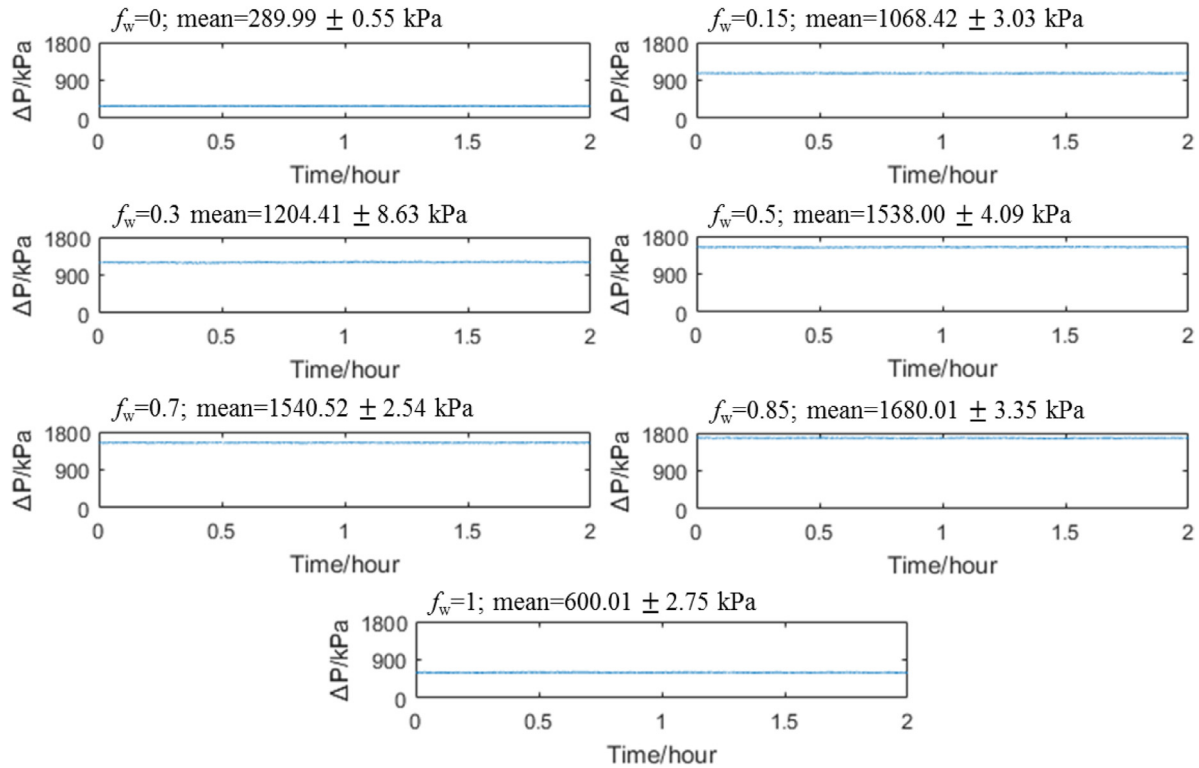


**Fig. 13.** Pressure difference measured between the inlet and outlet of the samples. The mean pressure drop and standard deviation at each fractional flow are shown.

when  $f_w = 0.5$ , the fraction of the pores occupied by the intermittent phase in the macro-pore space was 0.24 in Estaillades, while it was 0.33 in Bentheimer sandstone. The intermittent phase is seen mainly in the intermediate-sized and smaller macro-pores, as opposed to only the intermediate sized pores in a sandstone.

The physical explanation of intermittency is that the flowing fluids have sufficient energy to periodically open more conductive flow channels (Reynolds et al., 2017): at lower flow rates, there is insufficient energy to overcome the capillary pressure barriers that block short-cuts in the flow. In a carbonate, oil and brine are also present in micro-porosity,

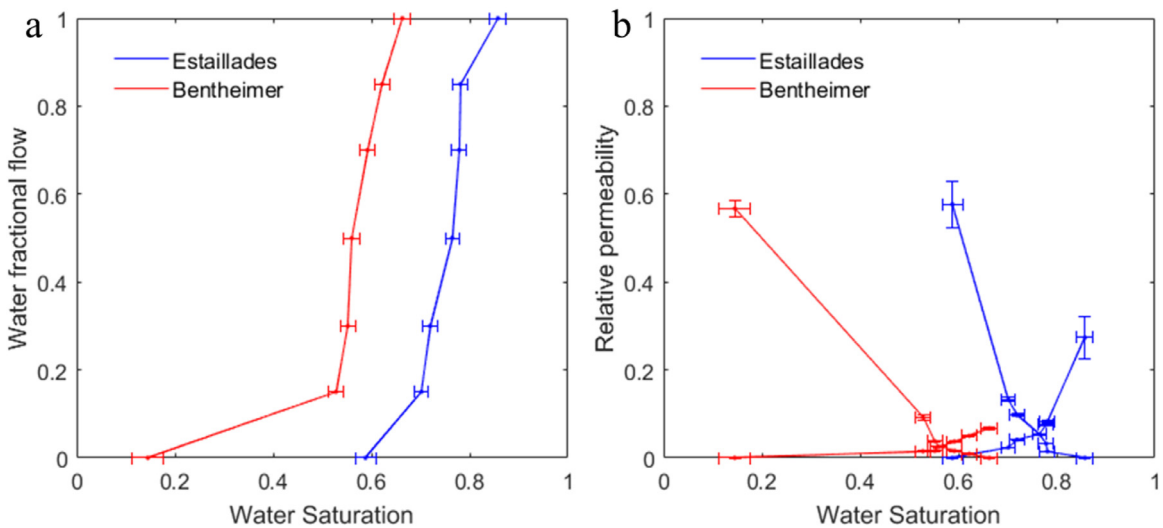


**Fig. 14.** (a) Fractional flow curves calculated at steady state for water (brine)-oil imbibition for Estaillades (blue) and Bentheimer (red) from Gao et al. (2017). (b) Relative permeability plotted as a function of wetting phase (water/brine) saturation in Estaillades and Bentheimer (Gao et al., 2017). Error bars in the x-direction consider uncertainties in the measured saturation caused by the threshold value chosen during image segmentation. Error bars in the y-direction consider uncertainties in the measurement of the length and diameter of the sample, the absolute permeability, pressure measurements, accuracy of pressure transducers and the pump rates. (For interpretation of the references to colour in this figure legend, the reader is referred to the web version of this article.)

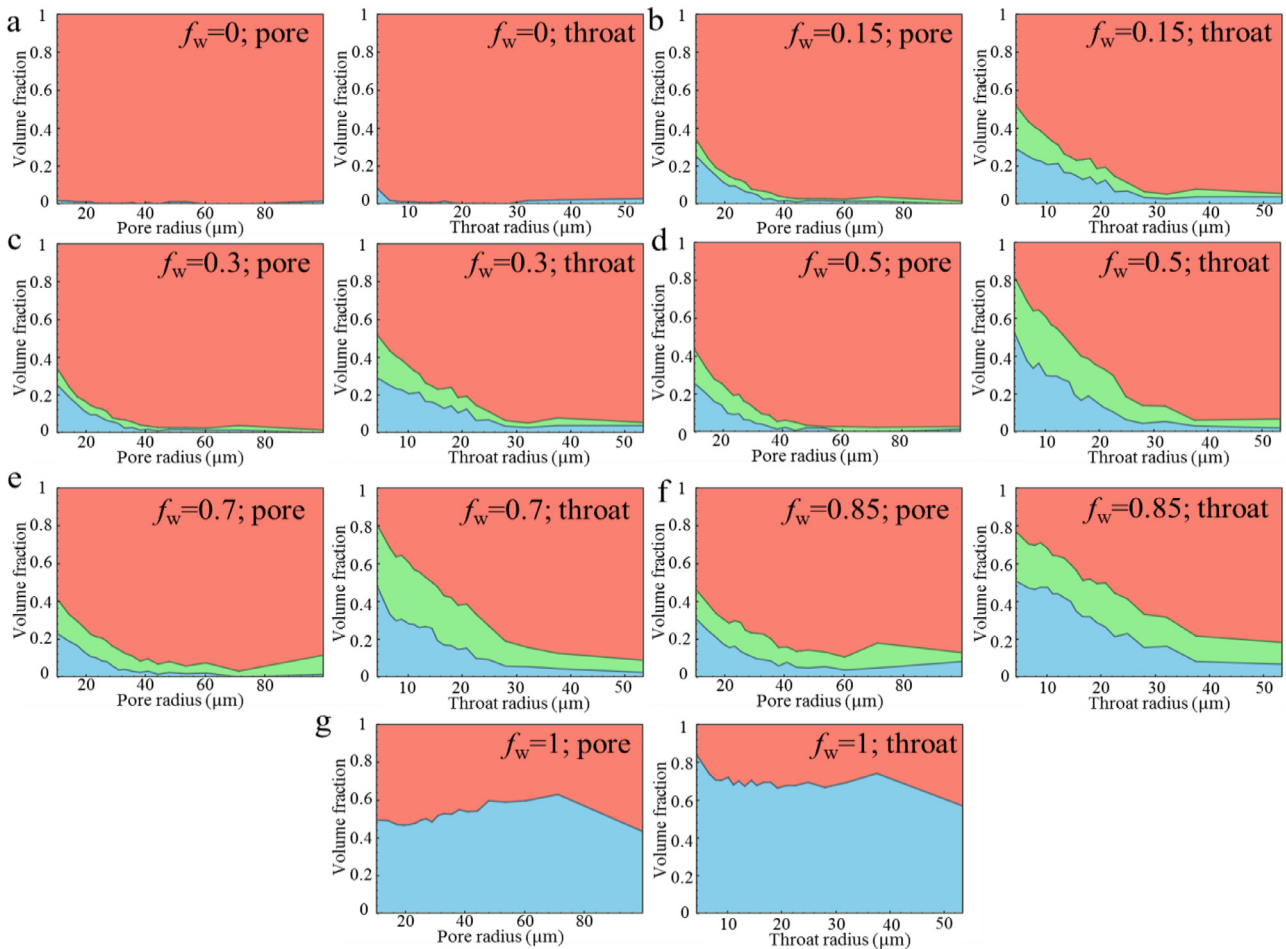


**Fig. 15.** The volume fraction of radii of pores and throats occupied by oil, brine and intermittent phases as a function of radius. Only the macro-pore space is considered in this analysis. Red represents oil, green is the intermittent phase, and blue is brine. (For interpretation of the references to colour in this figure legend, the reader is referred to the web version of this article.)

and so it is not surprising that even some of the smaller macro-pores allow intermittent connectivity at moderately high flow rates, facilitating flow through both the macro- and micro-porous regions.

#### 4. Conclusions

We have established a novel experimental and image analysis methodology to measure the pore occupancy, relative permeability and flow intermittency in a complex micro-porous carbonate. We have demonstrated this by conducting steady-state waterflood experiments on an Estaillades limestone sample at a capillary number,  $Ca = 7.3 \times 10^{-6}$  and performing differential imaging to distinguish macro-pore space, explicitly resolvable in the image, and micro-porosity, together with fluid occupancy.

Estaillades is a heterogeneous carbonate composed of approximately 27% solid grains, 7% macro-pores, and 66% micro-pores that could not be explicitly resolved from micro-CT images. We were able to quantitatively describe four phases: solid grain, pores occupied only by brine (micro-pore space I), micro-pores partially filled by oil and brine (micro-pore space II), and macro-pore space, which itself can contain oil, water or can be intermittent. During multiphase flow we could distinguish three types of fluid occupancy in the micro-pore space II: filled with oil, filled with brine, and partially-saturated with both brine and oil present. The micro-porosity contributed significantly to the total porosity: the fully brine-saturated portion of the pore space, approximately 57% of the total pore volume of the rock, contributed to a large initial brine saturation after primary drainage, shifting the relative permeabilities to the

right compared to Bentheimer sandstone. However, some of the micro-porosity, approximately 10% of the whole sample, initially contained oil that was displaced during waterflooding: the enhanced connectivity of the pore space through micro-porosity led to a higher end-point water relative permeability and a lower residual oil saturation than observed for a sandstone under similar conditions. Our method indicated initially relatively higher recovery from micro-porosity. This is expected in a water-wet rock where the wetting phase preferentially fills the smaller pores.

In the macro-pore space, the intermittent phase was identified by the differential imaging method, showing that there were some regions of the pore space that were occupied alternately by oil and brine. The intermittent phase was seen principally in the smaller and intermediate sized pores and the fraction of the pore space showing this fluctuating occupancy was slightly smaller than in Bentheimer sandstone under the same conditions.

This experimental technique is readily applicable to other systems in which micro-porosity plays an important role, including mixed-wet carbonates. Future work could include a wide variety of the pore-scale multiphase flow problems, including those at the conditions representative of subsurface aquifers, oil and gas fields and other deep geological systems.

#### Acknowledgements

We gratefully acknowledge funding from the Qatar Carbonates and Carbon Storage Research Centre (QCCSRC), provided jointly

by Qatar Petroleum, Shell, and the Qatar Science & Technology Park, and the Imperial College Consortium on Pore-Scale Modelling. The authors acknowledge Mr. Graham Nash, Dr. Edward Bailey, Dr. Saurabh Shan and Mr. Vincenzo Cunsolo for their assistance in the laboratory. The experimental data are available online at <https://www.bgs.ac.uk/services/ngdc/citedData/catalogue/f899eb2f-37a4-4dec-9b59-432f11250894.html>.

## References

- Aghaei, A., Piri, M., 2015. Direct pore-to-core up-scaling of displacement processes: dynamic pore network modeling and experimentation. *J. Hydrol.* 522, 488–509. <https://doi.org/10.1016/j.jhydrol.2015.01.004>.
- Akbarabadi, M., Piri, M., 2013. Relative permeability hysteresis and capillary trapping characteristics of supercritical CO<sub>2</sub>/brine systems: an experimental study at reservoir conditions. *Adv. Water Resour.* 52, 190–206. <http://dx.doi.org/10.1016/j.advwatres.2012.06.014>.
- Alyafei, N., Blunt, M.J., 2016. The effect of wettability on capillary trapping in carbonates. *Adv. Water Resour.* 90, 36–50. <https://doi.org/10.1016/j.advwatres.2016.02.001>.
- Andreas, J.M., Hauser, E.A., Tucker, W.B., 1938. Boundary tension by pendant drops1. *J. Phys. Chem.* 42 (8), 1001–1019.
- Armstrong, R.T., McClure, J.E., Berrill, M.A., Rücker, M., Schlüter, S., Berg, S., 2016. Beyond Darcy's law: the role of phase topology and ganglion dynamics for two-fluid flow. *Phys. Rev. E* 94, 43113. <https://doi.org/10.1103/PhysRevE.94.043113>.
- Arns, C.H., Baugé, F., Limaye, A., Sakellariou, A., Senden, T., Sheppard, A., Sok, R.M., Pinczewski, V., Bakke, S., Berge, L.I., Oren, P.E., Knackstedt, M.A., 2005. Pore Scale Characterization of Carbonates Using X-Ray Microtomography. <https://doi.org/10.2118/90368-PA>.
- Avraam, D.G., Payatakes, A.C., 1996. Flow regimes and relative permeabilities during steady-state two-phase flow in porous media. *Int. J. Multiph. Flow* 22, 127.
- Berg, S., Armstrong, R.T., Georgiadis, A., Ott, H., Schwinger, A., Neiteler, R., Brussee, N., Makurat, A., Rücker, M., Leu, L., Wolf, M., Khan, F., Enzmann, F., Kersten, M., 2015. Onset of oil mobilization and nonwetting-phase cluster-size distribution. *Petrophysics* 56, 15–22.
- Berg, S., Rücker, M., Ott, H., Georgiadis, A., van der Linde, H., Enzmann, F., Kersten, M., Armstrong, R.T., de With, S., Becker, J., Wiegmans, A., 2016. Connected pathway relative permeability from pore-scale imaging of imbibition. *Adv. Water Resour.* 90, 24–35. <http://dx.doi.org/10.1016/j.advwatres.2016.01.010>.
- Bijeljic, B., Mostaghimi, P., Blunt, M.J., 2013. Insights into non-Fickian solute transport in carbonates. *Water Resour. Res.* 49, 2714–2728. <https://doi.org/10.1029/wrcr.20238>.
- Bijeljic, B., Raeini, A.Q., Lin, Q., Blunt, M.J., 2018. Multimodal functions as flow signatures in complex porous media. *arXiv Prepr. arXiv 1807.07611*.
- Blunt, M.J., 2017. *Multiphase Flow in Permeable Media: A Pore-Scale Perspective*. Cambridge University Press.
- Blunt, M.J., Bijeljic, B., Dong, H., Gharbi, O., Iglauer, S., Mostaghimi, P., Paluszny, A., Pentland, C., 2013. Pore-scale imaging and modelling. *Adv. Water Resour.* 51, 197–216. <https://doi.org/10.1016/j.advwatres.2012.03.003>.
- Buades, A., Coll, B., Morel, J.-M., 2008. Nonlocal image and movie denoising. *Int. J. Comput. Vis.* 76, 123–139. <https://doi.org/10.1007/s11263-007-0052-1>.
- Buades, A., Coll, B., Morel, J.M., 2005. A non-local algorithm for image denoising. 2005 IEEE Comput. Soc. Conf. Comput. Vis. Pattern Recognit. <https://doi.org/10.1109/CVPR.2005.38>.
- Bultreys, T., Lin, Q., Gao, Y., Raeini, A.Q., AlRatrout, A., Bijeljic, B., Blunt, M.J., 2018. Validation of model predictions of pore-scale fluid distributions during two-phase flow. *Phys. Rev. E* 97, 53104. <https://doi.org/10.1103/PhysRevE.97.053104>.
- Burger, W., Burge, M.J., 2016. *Digital image processing: an algorithmic introduction using Java*. Springer.
- Chatenever, A., Calhoun Jr., J.C., 1952. Visual examinations of fluid behavior in porous media – part I. *J. Pet. Technol.* 4, 149–156. <https://doi.org/10.2118/135-G>.
- Datta, S.S., Dupin, J.-B., Weitz, D.A., 2014a. Fluid breakup during simultaneous two-phase flow through a three-dimensional porous medium. *Phys. Fluids* 26, 62004. <https://doi.org/10.1063/1.4884955>.
- Datta, S.S., Ramakrishnan, T.S., Weitz, D.A., 2014b. Mobilization of a trapped non-wetting fluid from a three-dimensional porous medium. *Phys. Fluids* 26, 22002.
- Gao, Y., Lin, Q., Bijeljic, B., Blunt, M.J., 2017. X-ray microtomography of intermittency in multiphase flow at steady state using a differential imaging method. *Water Resour. Res.* 53, 10274–10292. <https://doi.org/10.1002/2017WR021736>.
- Gharbi, O., Blunt, M.J., 2012. The impact of wettability and connectivity on relative permeability in carbonates: a pore network modeling analysis. *Water Resour. Res.* 48, <https://doi.org/10.1029/2012WR011877>.
- Ghous, A., Senden, T.J., Sok, R.M., Sheppard, A.P., Pinczewski, V.W., Knackstedt, M.A., 2007. 3D characterisation of microporosity in carbonate cores. *SPWLA Middle East Reg. Symp.*
- Gouze, P., Melean, Y., Le Borgne, T., Dentz, M., Carrera, J., 2008. Non-Fickian dispersion in porous media explained by heterogeneous microscale matrix diffusion. *Water Resour. Res.* 44. <https://doi.org/10.1029/2007WR006690>.
- Hussain, F., Pinczewski, W.V., Cinar, Y., Arns, J.Y., Arns, C.H., Turner, M.L., 2014. Computation of relative permeability from imaged fluid distributions at the pore scale. *Transp. Porous Media* 104, 91–107. <https://doi.org/10.1007/s11242-014-0322-7>.
- Johnson, E.F., Bossler, D.P., Naumann Bossler, V.O., 1959. Calculation of Relative Permeability From Displacement Experiments. *Pet. Trans. AIME* 216, 370–372.
- Kokkedee, J.A., Boom, W., Frens, A.M., Maas, J.G., 1996. Improved special core analysis: scope for a reduced residual oil saturation. In: Proceedings of the Annual Symposium of the Society of Core Analysts, Montpellier, France, September 8–10, paper SCA 1996-01, pp. 1–13.
- Lin, Q., Al-Khulaifi, Y., Blunt, M.J., Bijeljic, B., 2016. Quantification of sub-resolution porosity in carbonate rocks by applying high-salinity contrast brine using X-ray microtomography differential imaging. *Adv. Water Resour.* 96, 306–322. <http://dx.doi.org/10.1016/j.advwatres.2016.08.002>.
- Lin, Q., Bijeljic, B., Pini, R., Blunt, M.J., Krevor, S., 2018. Imaging and measurement of pore-scale interfacial curvature to determine capillary pressure simultaneously with relative permeability. *Water Resour. Res.* 54 (9), 7046–7060. <https://doi.org/10.1029/2018WR023214>.
- Lin, Q., Bijeljic, B., Rieke, H., Blunt, M.J., 2017. Visualization and quantification of capillary drainage in the pore space of laminated sandstone by a porous plate method using differential imaging X-ray microtomography. *Water Resour. Res.* 53, 7457–7468. <https://doi.org/10.1002/2017WR021083>.
- Mahani, H., Keya, A.L., Berg, S., Bartels, W.-B., Nasralla, R., Rossen, W.R., 2015. Insights into the mechanism of wettability alteration by Low-Salinity Flooding (LSF) in carbonates. *Energy Fuels* 29, 1352–1367. <https://doi.org/10.1021/ef5023847>.
- Norouzi Apourvari, S., Arns, C.H., 2016. Image-based relative permeability upscaling from the pore scale. *Adv. Water Resour.* 95, 161–175. <https://doi.org/10.1016/j.advwatres.2015.11.005>.
- Ott, H., Pentland, C.H., Oedai, S., 2015. CO<sub>2</sub>–brine displacement in heterogeneous carbonates. *Int. J. Greenh. Gas Control* 33, 135–144. <https://doi.org/10.1016/j.ijggc.2014.12.004>.
- Pak, T., Butler, I.B., Geiger, S., van Dijke, M.I.J., Sorbie, K.S., 2015. Droplet fragmentation: 3D imaging of a previously unidentified pore-scale process during multiphase flow in porous media. *Proc. Natl. Acad. Sci.* 112, 1947–1952. <https://doi.org/10.1073/pnas.1420202112>.
- Payatakes, A.C., 1982. Dynamics of oil ganglia during immiscible displacement in water-wet porous media. *Annu. Rev. Fluid Mech.* 14, 365–393.
- Prodanović, M., Mehmani, A., Sheppard, A.P., 2015. Imaged-based multiscale network modelling of microporosity in carbonates. *Geol. Soc. London, Spec. Publ.* 406 95 LP–113.
- Raeini, A.Q., Bijeljic, B., Blunt, M.J., 2017. Generalized network modeling: network extraction as a coarse-scale discretization of the void space of porous media. *Phys. Rev. E* 96, 13312. <https://doi.org/10.1103/PhysRevE.96.013312>.
- Reynolds, C.A., Menke, H., Andrew, M., Blunt, M.J., Krevor, S., 2017. Dynamic fluid connectivity during steady-state multiphase flow in a sandstone. *Proc. Natl. Acad. Sci.* 114 (31), 8187–8192 201702834.
- Rücker, M., Berg, S., Armstrong, R., Georgiadis, A., Ott, H., Simon, L., Enzmann, F., Kersten, M., de With, S., 2015a. The fate of oil clusters during fractional flow: trajectories in the saturation–capillary number space. Proceedings of the Annual Symposium of the Society of Core Analysts, Newfoundland and Labrador, Canada, August 14–21, paper SCA 2015-007.
- Rücker, M., Berg, S., Armstrong, R., Georgiadis, A., Ott, H., Schwinger, A., Neiteler, R., Brussee, N., Makurat, A., Leu, L., Wolf, M., Khan, F., Enzmann, F., Kersten, M., 2015b. From connected pathway flow to ganglion dynamics. *Geophys. Res. Lett.* 42, 3888–3894. <https://doi.org/10.1002/2015GL064007>.
- Sinha, S., Bender, A.T., Danczyk, M., Keepseagle, K., Prather, C.A., Bray, J.M., Thrane, L.W., Seymour, J.D., Codd, S.L., Hansen, A., 2017. Effective rheology of two-phase flow in three-dimensional porous media: experiment and simulation. *Transp. Porous Media* 119, 77–94. <https://doi.org/10.1007/s11242-017-0874-4>.
- Sinha, S., Hansen, A., 2012. Effective rheology of immiscible two-phase flow in porous media. *EPL (Europhys. Lett.)* 99 (4), 44004.
- Stauffer, C.E., 1965. The measurement of surface tension by the pendant drop technique. *J. Phys. Chem.* 69 (6), 1933–1938.
- Tallakstad, K.T., Lovoll, G., Knudsen, H.A., Ramstad, T., Flekkøy, E.G., Maløy, K.J., 2009. Steady-state, simultaneous two-phase flow in porous media: an experimental study. *Phys. Rev. E* 80, 36308. <https://doi.org/10.1103/PhysRevE.80.036308>.
- Tian, Z., Wang, J., 2018. Lattice Boltzmann simulation of dissolution-induced changes in permeability and porosity in 3D CO<sub>2</sub> reactive transport. *J. Hydrol.* 557, 276–290. <https://doi.org/10.1016/j.jhydrol.2017.12.037>.
- Turner, M.L., Knüfig, L., Arns, C.H., Sakellariou, A., Senden, T.J., Sheppard, A.P., Sok, R.M., Limaye, A., Pinczewski, W.V., Knackstedt, M.A., 2004. Three-dimensional imaging of multiphase flow in porous media. *Phys. A Stat. Mech. Appl.* 339, 166–172. <https://doi.org/10.1016/j.physa.2004.03.059>.
- Wildenschild, D., Sheppard, A.P., 2013. X-ray imaging and analysis techniques for quantifying pore-scale structure and processes in subsurface porous medium systems. *Adv. Water Resour.* 51, 217–246. <http://dx.doi.org/10.1016/j.advwatres.2012.07.018>.
- Zou, S., Armstrong, R.T., Arns, J.-Y., Arns, C.H., Hussain, F., 2018. Experimental and theoretical evidence for increased ganglion dynamics during fractional flow in mixed-wet porous media. *Water Resour. Res.* 54 (5), 3277–3289. <https://doi.org/10.1029/2017WR022433>.